Heliyon 11 (2025) e42238

Contents lists available at ScienceDirect

Heliyon

journal homepage: www.cell.com/heliyon

Research article

CADD-based discovery of novel oligomeric modulators of PKM2 with antitumor activity in aggressive human glioblastoma models

Maia Cabrera [a,*,1], Romina Armando [b,1], Ian Czarnowski [a], Patricio Chinestrad [a], Ramiro Blanco [a], Alejandra Zinni [a], Daniel Gómez [b], Diego L. Mengual Gómez [b], Pablo Lorenzano Menna [a]

[a] *Laboratorio de Farmacología Molecular, Departamento de Ciencia y Tecnología, Universidad Nacional de Quilmes, Argentina*
[b] *Unidad de Oncología Molecular, Centro de Oncología Molecular y Traslacional, Departamento de Ciencia y Tecnología, Universidad Nacional de Quilmes, Argentina*

ARTICLE INFO

Keywords:
PKM2
Pharmacological inhibitors
Docking based virtual screening
Molecular dynamics

ABSTRACT

Pyruvate kinase isoform M2 (PKM2) is a multifunctional enzyme capable of transitioning between monomeric, dimeric, and tetrameric states, with its oligomeric equilibrium playing a pivotal role in tumour progression and survival. The unique exon ten at the dimer-dimer interface represents an attractive target for isoform-specific modulation, offering opportunities for disrupting this equilibrium and altering tumour cell dynamics.

This study identifies a novel druggable pocket at the PKM2 dimer interface through conformational analysis. This pocket was exploited in a virtual screening of a large small-molecule library, identifying two promising candidates, C599 and C998. Both compounds exhibited dose-dependent antiproliferative effects in glioblastoma cell lines and induced apoptosis, as evidenced by caspase 3/7 activation. These effects were directly linked to their inhibition of PKM2 enzymatic activity, validating the proposed mechanism of action in their rational design. ADMET studies further highlighted their strong potential as lead PKM2 inhibitors for GBM treatment.

Molecular dynamics (MD) simulations and post-MD analyses, including Dynamic Cross-Correlation Maps (DCCM), Probability Density Function (PDF), and Free Energy Landscape (FEL), confirmed the stability of the protein-ligand interactions and highlighted critical residues at the dimer-dimer interface. The Steered MD simulations demonstrated the high affinity of the compounds for PKM2, as evidenced by the requirement of high rupture forces to induce an unbinding event. These results highlight the potential of the compounds as oligomeric modulators of PKM2. These findings position C599 and C998 as promising lead compounds for antitumor applications. Future studies will focus on optimising these candidates and assessing their efficacy *in vivo* glioblastoma models, reassuring the thoroughness of our research and the potential for further advancements.

* Corresponding author.
E-mail address: maia.cabrera@unq.edu.ar (M. Cabrera).
[1] Both authors contributed equally to this work.

https://doi.org/10.1016/j.heliyon.2025.e42238
Received 29 October 2024; Received in revised form 22 January 2025; Accepted 22 January 2025
Available online 24 January 2025

1. Introduction

Modifying quaternary structure dynamics is an emerging strategy for rational drug design. Numerous proteins known as morpheeins have demonstrated that physiological assembly and disassembly of alternate conformations are directly linked with multifunctional activities (moonlighting) and subcellular localisation [1]. Consequently, shifting the equilibrium of these conformations is tightly regulated, and any deviation can significantly impact cellular responses. In the context of drug design, this provides a novel model for allosteric regulation, as displacing the equilibrium could alter cellular responses independent of physiological stimuli [2].

One metabolic protein exhibiting moonlighting activities related to multimeric conversion is isoform 2 of the glycolytic enzyme pyruvate kinase (PKM2) [3]. PKM2 converts phosphoenolpyruvate (PEP) to pyruvate and plays an important role in the Warburg effect, a metabolic shift in cancer cells.

PKM2 is one of four isoforms of pyruvate kinase expressed in mammalian cells and, like PKM1, is encoded by the PKM gene [4]. While both PKM1 and PKM2 share the same length, they differ by 22 amino acids encoded by exon 10, which are located within two α-helices, Cα1 and Cα2, at the C-terminal domain of PKM2 (Fig. 1A and B) [5,6].

Each subunit (monomer) of the tetramer consists of four domains designated A, B, C, and D. The dimer forms through the association of two PKM2 monomers via their A-A′ interface. In contrast, the tetramer arises from the interaction of two dimers along the C-terminal domains [6]. Unlike PKM1, the M2 isoform oscillates between low glycolytic activity as a monomer/dimer and high enzymatic activity in the tetrameric conformation [6].

While canonical PKM2 activity promotes ATP production in its tetrameric state, the monomer/dimer conformations exhibit multiple non-canonical activities, such as channelling glucose-derived carbons toward anabolism, acting as co-transcriptional activators, or exhibiting kinase activity (Fig. 2). Thus, the dimer-tetramer equilibrium is tightly regulated by numerous mechanisms, including ligand-induced allosteric regulation, several post-translational modifications [7], and direct interactions with oncogenic proteins [8]. The tetramer also undergoes an allosteric transition from a low-affinity (T-state) to a high-affinity (R-state) conformation upon substrate binding, adding further complexity to its regulatory mechanisms.

Given its role in metabolic reprogramming and cell cycle progression, it is unsurprising that PKM2 expression patterns predominate in tissues exhibiting high anabolic functions, such as embryonic and tumour cells [9]. Thus, regulating the equilibrium with small molecules could interfere with its canonical or non-canonical activity. Regardless of the strategy employed, decreasing its activities could significantly impact tumour cell requirements and potentially induce cytotoxicity.

Several small molecules have been identified as either activators or inhibitors of PKM2 [10,11]. Their mechanisms of action include stabilising the protein in a fully active tetrameric conformation [12], locking it in the dimeric state, or inducing allosteric modulation [10].

GBM is the most common and higher-grade malignant (grade IV) brain tumour in adult and aged individuals. With more than 60 % of incidence in adults [13] and a median overall survival of 15 months after diagnosis, searching for novel therapeutic approaches is a crucial public health issue [14–16].

GBM tumours exhibited extreme cell proliferation, angiogenesis, high resistance to apoptosis and chemoresistance [17,18] all characteristics related to canonical and non-canonical activities of PKM2 (Fig. 2).

Among the identified PKM2 inhibitors, two naturally occurring compounds Shikonin [19] and Gliotoxin [20] demonstrated anti-tumour activity in glioblastoma models. Both compounds induce apoptosis by suppressing PKM2-mediated aerobic glycolysis, generating reactive oxygen species (ROS) and regulating PKM2/STAT3 signal pathway [21,22]. However, the specific regions or residues responsible for the compounds-PKM2 interaction remain unidentified. These findings highlight PKM2 as a promising therapeutic target in glioma, where inhibiting its activity through small molecules could offer novel approaches to hinder tumour growth and progression.

In this study, we aim to apply computer-aided drug design (CADD) strategies to develop novel modulators of PKM2's canonical activity by disrupting the natural balance of its oligomeric states. To achieve this, we utilised a docking-based virtual ligand library screening and *in vitro* evaluation, followed by molecular dynamics simulations to evaluate the interactions and stability of promising candidates.

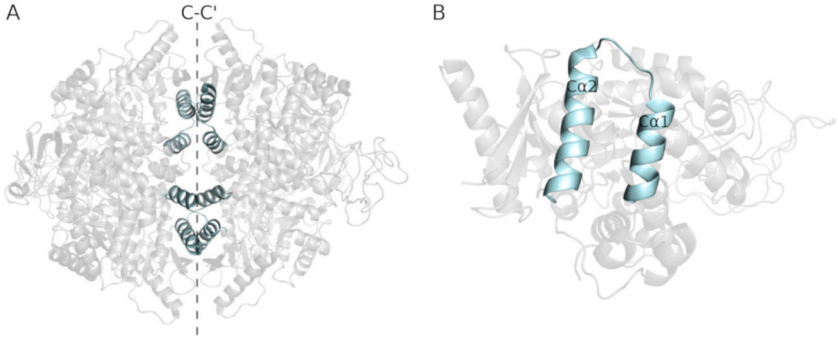

Fig. 1. (A). PKM2 Tetrameric conformation. The tetramer is the association of a pair of dimers along the C terminal domain of each monomer. (B). The PKM2-specific 22 amino acids encoded by exon 10 are within the two α helices, Cα1 and Cα2 (light green).

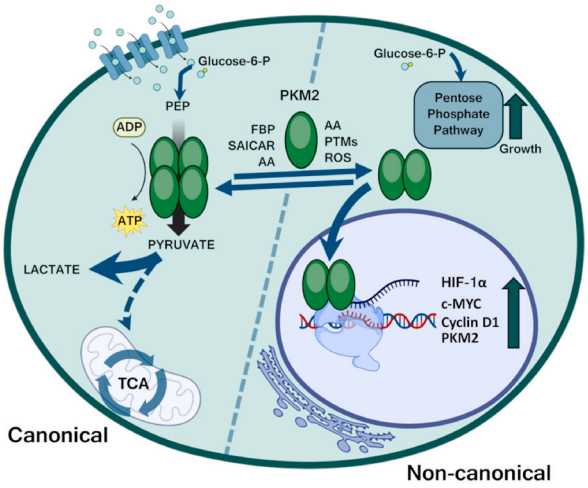

Fig. 2. Metabolic reprogramming in glioblastoma cells driven by PKM2. Glioblastoma cells exhibit increased energy production and biosynthetic demands, leading to anaerobic glycolysis (the Warburg effect) even in the presence of oxygen [70]. This metabolic reprogramming is facilitated by several key mechanisms involving both canonical and non-canonical activities of PKM2: a) upregulation of glucose transporters (GLUTs) and PKM2 facilitates increased glucose conversion to pyruvate, leading to elevated lactate production [71,72]; b) excess lactate suppresses antitumor immune responses, promotes extracellular acidosis, and contributes to tumour growth, progression, and therapy resistance; c) glycolytic intermediates are redirected to the pentose phosphate pathway (PPP) to provide amino acids and nucleotides necessary for cancer cell proliferation; d) dimeric PKM2 migrates to the nucleus, where it activates oncogenic transcription factors that regulate proliferation, angiogenesis, tumorigenesis, and epigenetic modifications and PKM2 expression [73,74]; e) mitochondrial translocation of PKM2 protects GBM cells from oxidative stress-induced apoptosis through Bcl-2 phosphorylation [75]. Finally, PKM2 conformational dynamics is tightly regulated by numerous mechanisms including ligand-induced allosteric regulation (fructose bisphosphate (FBP), amino acids, Succinyl amino imidazole carboxyamide ribose-5-phosphate (SAICAR), several post-translational modifications (PMTs) and reactive species oxygen (ROS).

Docking protocols are widely used due to their speed and low computational demand. However, since these methods primarily consider proteins as rigid structures, integrating conformational analysis of the protein target increases the accuracy of predicted protein-ligand interactions. Additionally, molecular dynamics (MD) simulations offer a powerful complement to docking by providing a more detailed and dynamic system representation.

As a morpheein protein, PKM2 contains unique amino acids within the dimer-dimer interface, providing a prime opportunity for allosteric regulation. Additionally, targeting these unique sequences may facilitate the identification of small molecules selective for the M2 isoform of PK. To explore this possibility, we focused on the C-C′ interface to conduct a detailed analysis of the conformational diversity of PKM2. We considered all available crystallographic structures deposited in the Protein Data Bank (https://www.rcsb.org/) [23] and analysed the dimer interface using the "Protein Interfaces, Surfaces and Assemblies" (PISA) server [24,25] (https://www.ebi.ac.uk/msd-srv/prot_int/pistart.html).

We identified and characterised a druggable pocket within the C-C′ interface, which became the focal point of our high-throughput virtual library screening using Autodock Vina as the docking software and a library of approximately 500,000 drug-like compounds. This pocket, due to its unique structural and functional properties, presents a promising target for the development of PKM2 modulators.

The preliminary *in vitro* evaluation in GBM cell lines showed that two candidates, C599 and C998, inhibited proliferation, induced caspase-3/7 enzymatic activity and decreased the pyruvate activity of PKM2 in a dose-dependent manner across glioblastoma cell lines. These results suggest a potential to interfere with the metabolic reprogramming characteristic of glioblastoma cells [18,26]. To investigate these interactions further, we conducted a detailed molecular dynamics (MD) analysis of the binding of the identified ligands to PKM2. Moreover, we performed steered molecular dynamics (SMD) simulations to measure the interaction forces between the compounds and PKM2, providing insights into the stability and strength of these interactions.

Thus, the strategy assessed in the present work enabled the identification of a suitable lead candidate for altering the fine-tuned modulation of PKM2, representing a potential novel strategy to interfere with PKM2's tumour-related cellular functions. Further analysis of the candidate and its effects on other PKM2-related pathways will help us determine its potential in the context of glioblastoma.

2. Material and methods

2.1. PKM2 conformational diversity analysis and interface characterisation

The human Pyruvate kinase (PKM) crystal structures were retrieved from the Protein Data Bank (PDB) according to the following criteria [27]. A total number of one hundred and sixty-three (163) conformations were used for the analysis excluding structural

mutants and considering resolution better than 3 Å. The single-point mutant conformations were considered for the analysis: The S437Y mutant, activated by Serine but unable to bind FBP (PDBid: 3G2G); the Y105E mutant (PDBid: 4QG6); the K305Q mutant (PDBid: 4QG8); the H391Y mutant (PDBid: 4YJ5); the R399E mutant (PDBid: 4QG9); the K422R mutant (PDBid: 4QGC) and the C424A mutant (PDBid: 4WJ8). Global Root-mean-square deviation (RMSD) between all conformers was calculated using the Mammoth [28] software. The Z-Scores derived from each C-alpha RMSD were calculated using the MacLachlan algorithm implemented in the ProFit software (http://www.bioinf.org.uk/software/profit/) [29]. For further analysis, the crystal structure PDB ID: 4B2D [30] was selected, and the C-C' interface was examined using the PISA service [24] via the CCP4 software suite 9.0 [25] https://cloud.ccp4.ac.uk/.

2.2. Druggable pocket prediction

The identification and characterisation of cavities on the C-C′ interface of 4B2D were performed using Fpocket software (https://fpocket.sourceforge.net/). This software applies an algorithm based on Voronoi tessellation to detect protein cavities and informs several physicochemical parameters of said cavities, such as volume, druggability score, hydrophobicity and polarity [31].

2.3. Molecular docking and virtual screening workflow

The crystal structure of PKM2 (PDB ID: 4B2D) was retrieved from the Protein Data Bank (PDB). Chain D was selected for subsequent molecular docking and molecular dynamics simulations. Protein and ligand preparations were carried out using AutoDockTools. For protein preparation, co-crystallized water molecules were removed to avoid interference with ligand docking. Polar hydrogens were added to account for hydrogen-bonding interactions, and Gasteiger charges were assigned to ensure proper charge distribution across the protein structure. The structures of ligands were prepared automatically using Autotors, which define rotatable bonds and ensure ligand flexibility during the docking process. Ligands were further minimised using default parameters in ADT to optimise their geometry.

For docking-based virtual screening (DBVS), a 3D grid was defined in ADT, centred on the α-carbon of residue Cys424 within the novel pocket. Residue Cys424 was chosen as the grid centre because it is specific to PKM2 and determines the different catalytic and modulatory properties between PKM splicing isoforms. The grid dimensions were set to 24 × 20 × 18 Å, with a grid spacing of 1 Å, ensuring sufficient coverage of the binding site. The exact grid centre coordinates were (37.095 Å, −2.003 Å, 22.85 Å).

The ligand library for DBVS was sourced from the publicly available Enamine Advanced Collection, which contains over 500,000 drug-like compounds with predefined criteria: molecular weight $\leq$350 Da, cLogP $\leq$3, and $\leq$7 rotatable bonds. This library was accessed online via the Enamine website (https://www.enamine.net).

Docking calculations were performed using AutoDock Vina, a robust docking engine that combines grid-based scoring with a stochastic global optimization algorithm. Each ligand was subjected to flexible docking within the predefined grid. Vina generated up to nine binding poses for each ligand, ranked by their binding energy scores.

The docking poses were visually inspected using PyMOL and ADT to identify the most promising compounds based on their orientation, interactions with key residues (e.g., Cys424, Arg489), and docking scores. The top ten candidates with the most favourable docking scores (i.e., lowest binding energies) were selected for further evaluation. Chemical diversity analysis was performed to ensure structural variability among the selected compounds, avoiding redundancy in their chemical scaffolds.

2.4. Chemical diversity of the compounds

To maximise the chemical diversity among the candidate molecules, the similarity between molecules was estimated by applying two types of fingerprints. First, the 1024-bit Morgan 2D fingerprints, with a radius of 2, were calculated using the RDKIT implementation (http://www.rdkit.org). Furthermore, the 166 Molecular Access System (MACCS) Keys implemented in RDKit were calculated [32]. The chemical structures of the top ten ranking compounds are provided in Supplementary Fig. S1.

2.5. Cell culture

Human glioblastoma cell lines LN299 and U87 were obtained from ATCC, cataloge number CRL-2611 and HTB-14 respectively. U251 cell lines were obtained from Sigma, cataloge number 09063001. Culture media (DMEM, Dulbecco's modified Eagle's medium) was obtained from Gibco, Thermo Fisher Scientific, Argentina. Dimethylsulfoxide (DMSO) was procured from Interchemistry, Argentina. Fetal bovine serum (FBS) was obtained from Natocor, Argentina. The culture-grade plastic wares were obtained from Abcam, Argentina. Cells were cultured in Dulbecco's modified Eagle's medium supplemented with 10 % FBS and 100 mg/mL streptomycin and maintained under a humidified atmosphere containing 5 % CO_2 at 37 °C. Confluent cell cultures were washed with phosphate buffer saline (PBS, pH 7.4) and then subcultured twice a week, trypsin 0,05 % in saline was used for harvesting cells. Cell lines were tested for mycoplasma contamination twice a year.

2.6. Cell proliferation assay

Cell proliferation was determined by a colourimetric assay using CellTiter 96 AQueous Non-Radioactive Cell Proliferation Assay (Promega, USA) according to the manufacturer's instructions. For the MTS assay, cells growing in the exponential phase were seeded at 2.0×10^4 cells/well in a 96-well plate and incubated in an atmosphere of 5 % CO_2 at 37 °C. Prior to treatment, cells were given a 24h

period to settle. The synthetised compounds were solubilised in culture grade DMSO and added to the cell culture medium. Cells were exposed to serial dilutions of Hit1-10 or 0.1 % (v/v) DMSO (vehicle control group). After incubation for 48h, 20 μl of MTS was added to each well, followed by a 30 min incubation at 37 °C. Absorbance was measured at 490 nm using the FlexStation 3 microplate reader (Molecular Devices Inc., USA).

Half maximal inhibitory concentration 50 (IC_{50}) values were calculated with GraphPad Prism software (GraphPad Software Inc., USA) using the sigmoidal dose-response function and expressed as IC_{50} (μM). Assays were carried out in triplicate and at least three independent experiments were conducted.

2.7. PKM2 activity assay

Pyruvate kinase activity was measured according to the manufacturer's instructions. Briefly, U87 cells were grown in 96 well culture plates at densities estimated to yield 80 % confluence within 24h of incubation in the aforementioned conditions. Then, the medium was replaced with fresh DMEM for 1 h before 2 h treatment with C599 and C998 compounds. Control cells were treated with DMSO as vehicle control. Pyruvate kinase activity in lysates was determined by the Pyruvate Kinase activity assay kit (MAK072, Sigma Aldrich). Results are represented as mean and standard deviation (SD) of at least three independent experiments.

2.8. Caspase 3/7 activity assay

Following vendor's protocol, apoptosis assay was performed on U87 using Caspase-Glo® 3/7 Assay System (Promega, USA, Cataloge Number: G8090). Apoptosis assay Caspase-Glo® 3/7 reagent was prepared by adding Caspase-Glo® 3/7 buffer and Caspase-Glo® 3/7 substrate and mixing until the substrate was thoroughly dissolved. Cells were seeded on a 96-well plate at a density of 1.0×10^4 and incubated overnight in DMEM culture media with 10 % FBS. The next day, the media was replaced with serum-free DMEM and cells were starved for 12h. After starvation, cells were treated with the compounds at concentrations similar to their respective IC_{50} concentration for 24h, then, cells were incubated with Apoptosis assay Caspase-Glo® 3/7 reagent for 30 min in the dark. Finally, the reagent was collected and transferred to a white-walled 96-well plate, and luminescence was measured using the FlexStation 3 microplate reader (Molecular Devices Inc., USA). Data was then analysed with GraphPad Prism software (GraphPad Software Inc., USA). Results are represented as mean and standard deviation (SD) of at least three independent experiments.

2.9. In silico ADMET property prediction

The pharmacokinetic properties i.e., absorption, distribution, metabolism, and excretion (ADME) of the ten selected compounds were analysed using the pkCSM toxicity prediction tool [33]. The ten ranking molecules were also predicted for their *in silico* toxicity in order to improve their safety for therapy and to reduce clinical failures in drug development.

2.10. Molecular dynamic simulation setup

Several MD simulations were performed to elucidate the dynamics of PKM2 both alone and in complex with C599 and C998. The MD systems were prepared consistently across all cases and a 100 ns simulation was conducted using GROMACS version 2024 [34]. The CHARMM36m forcefield [35] was chosen for all simulations. The compound's topology generation and parameter assignment of the compounds were carried out using CGenFF [34].

Each system was embedded in a dodecahedral periodic cell with a minimum distance of 1 nm from the protein to the box edge to satisfy the minimum image convention. The CHARMM36m modified TIP3P water model was used to solvate the systems [36]. Sodium and chloride ions were added to neutralise the system's net charge and achieve a physiological concentration of 150 mM.

Conditioning of the systems consisted of an initial energy minimisation step of 50,000 steps followed by temperature and pressure equilibration. The systems were heated to 310 K in 100 ps using position-restrained molecular dynamics simulations. Afterwards, the system was equilibrated to 310 K and 1 bar as an isothermal-isobaric ensemble. The V-rescale thermostat and the C-rescale pressure coupling algorithms were used. The hydrogen bonds were constrained by the LINCS algorithm [37]. Neighbour searching was performed using the Verlet cut-off scheme, and the neighbour list was updated every ten steps. The Coulombic and Lennard-Jones interactions cut-off distance was of ten Å. The long-range electrostatic interactions were calculated using the Particle-mesh Ewald method [38]. For all simulations, a two fs step size was used.

The RMSD and Hydrogen Bond count resulting from the MD of each system were computed using the rms and hbond tools implemented in GROMACS 2024.

2.11. Dynamic cross-correlation map (DCCM) and probability density function (PDF) analysis

The cross-correlation map of the movement of alpha carbons observed during MD simulations shows both the correlated and anticorrelated movements of the protein residues [39]. For each 100 ns MD simulation of free PKM2 and PKM2 in complex with C599 and C998, the DCCM was calculated using the Bio3D package [40].

The kernel density estimation (KDE)-based probability density function (PDF) analysis evaluates the frequency likelihood of trajectory events in molecular dynamics (MD) simulations [41,42]. In this study, the PDF analysis for each simulation was conducted using the Geo_Measures v0.9 [43] plugin within the PyMOL software (The PyMOL Molecular Graphics System, Version 3.0,

Schrödinger, LLC).

2.12. Free energy landscape determination and 2D interaction diagram

For the PKM2-C599 and PKM2-C998 systems, the Free Energy Landscape (FEL) was determined from the respective 100 ns simulations. To this end, the first and second Principal Components (PCs) were calculated using the principal component analysis (PCA) method. First, the covariance matrix was calculated using the protein backbone for least squares fitting and the eigenvectors were obtained. Subsequently, we calculated the projections of the data trajectories onto the first and second PCs, which correspond to the first and the second eigenvectors of the covariance matrix. From the previously calculated PCs, each FEL was determined. Finally, a snapshot of each system at the energy minimum was extracted, as identified by the Free Energy Landscape.

The covariance matrix, projections and FELs were determined using the covar, anaeig and sham tools implemented in GROMACS 2024.

The 2D interaction diagrams for both PKM2-C599 and PKM2-C998 complexes at their respective global energy minima were determined using the Schrodinger Maestro software https://www.schrodinger.com/platform/products/maestro/(Schrödinger Release 2024-3: Maestro, Schrödinger, LLC, New York, NY, 2024).

2.13. Steered MD simulation setup

Steered Molecular Dynamics (SMD) is a powerful computational technique widely used in the study of protein-ligand interactions. This method consists of applying an external force to the system, to explore the processes and pathways involved in the binding and unbinding of ligands [44,45].

Furthermore, the rupture force, which is the maximum force applied to the ligand that unbinds it from its pocket, highly correlates with experimental binding energies [46]. Compared to other computational techniques to infer the binding affinity of ligands, SMD is relatively inexpensive to perform computationally.

The preparation of the system for the SMD simulations was identical to the previously described MD simulation, except for the periodic cell being a rectangle extended in the Z axis sufficiently to allow for the pulling of C4 without infringing the minimum-image convention. After the equilibration steps, five SMD simulations were conducted starting with the equilibrated configuration. For the SMD simulations, the Nose-Hoover thermostat [47,48] and the Parrinello-Rahman barostat [49,50] were used. Restraints were removed only from C4, while the protein was used as an immobile reference for the pulling simulations. A force was applied to the Center of Mass (COM) of C4 along the Z axis for a total of 2 ns using a spring constant of 5 kcal mol-1 Å-2 and a pull rate of 0.01 nm ns-^{1} [51]. This allows sufficient time for the ligand to completely exit the protein pocket into the bulk of the solvent. The average rupture force was calculated from all five simulations.

2.14. Statistical analysis

All data are represented as mean ± standard deviation (SD). The statistical significance of differences between groups was assessed using one-way analysis of variance (ANOVA) followed by Dunnett's post-hoc tests. All analyses were performed using GraphPad Prism 6 software, with statistical significance defined as $p < 0.05$.

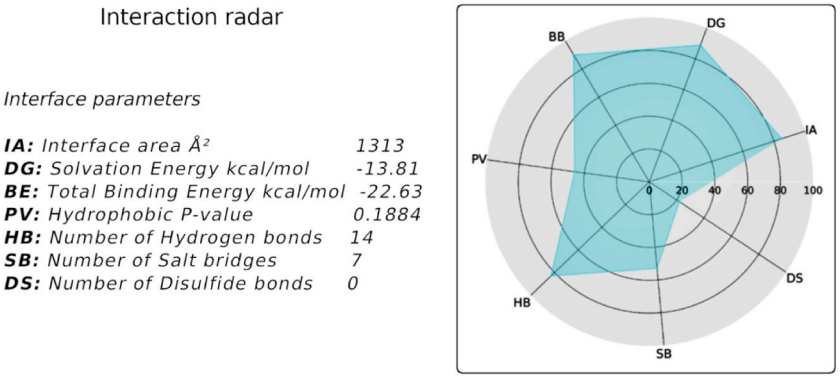

Fig. 3. Interaction radar plot graphic and Interface physicochemical parameters. The radar area exceeding the 50 % borderline at most points indicates that the interface is not a crystal packing artefact.

3. Results

3.1. Conformational analysis, characterisation of the dimer-dimer interface, and identification of a druggable pocket

Most of the crystal structures deposited in the PDB exhibit a tetrameric configuration, although some correspond to PKM2 variants described as a monomer/dimer mixture in biochemical and biophysical assays [52]. To study the mobility range of the residues involved in the C-C′ interface we conducted an exhaustive conformational analysis of all the crystal structures of PKM2 available in PDB. Those structures with mutations were excluded from the analysis. From 163 monomers, the conformers displaying the greatest difference (maximum pair) were the 3SRH chain B and 4FXF chain D with an RMSD of 4.23 Å. Both structures belong to tetrameric structures without mutations indicating that dimer-dimer contact is located in a low mobility region within the C-C' interface contributing to the idea that this region is an appropriate target to interfere with small molecules.

As PKM2 is a homotetramer, all monomers at the dimer-dimer interface possess the same pocket. Since C-C' interface did not show significant structural flexibility the chain D of PKM2 active conformation PDB ID 4B2D was selected as the template for further characterisation of the dimer-dimer interface.

We obtained detailed information about protein-protein interfaces' structural and biochemical characteristics using the PDBePISA tool, an interactive tool for exploring macromolecular interface characteristics. One of the most important applications of PISA software is its ability to identify potential misinterpretations regarding the structural and chemical nature of interfaces, which could be caused by crystal packing. In this context, the results of the analysis confirmed that the values correspond to a biologically relevant interface, ruling out the possibility of an artefact due to crystal packing (Fig. 3). Additionally, the dimer-dimer interface analysis revealed that 36 residues from each chain are involved, with 24 of these residues encoded by exon 10 forming the Cα1 and Cα2 helices of PKM2. With a buried surface area (BSA) of 1313.1 $Å^2$ and a hydrophobic P-value of 0.1884, this interface is smaller than the monomer-monomer contact and includes 14 hydrogen bonds and seven salt bridges.

The Z-score derived from Carbon-alpha RMSD per position of residues within the pocket showed higher structural stability (Fig. 4A) in comparison with the B domain previously reported as highly mobile [6]. We used the software F-pocket to identify a druggable pocket in the C-C′ interface surface [31]. The analysis of the region showed a cavity within the C-C′ interface with a volume of 655, 12 $Å^3$, and a hydrophobicity score of 29.44 (Fig. 4B and C). These results indicate that residues in the identified pocket contact are located in the low mobility region within the C-C' interface.

3.2. DBVS for ligands targeting the characterised druggable pocket at the PKM2 dimer-dimer interface

The candidates obtained from the DBVS using the library "Advanced Collection from Enamine" were ranked based on the docking scores. The scoring function corresponds to the binding affinity of the ligand-protein complex and, therefore, is an indicator of the predicted best binders. An initial examination of the top-ranked candidates (Supplementary Fig. S1) revealed estimated energy binding

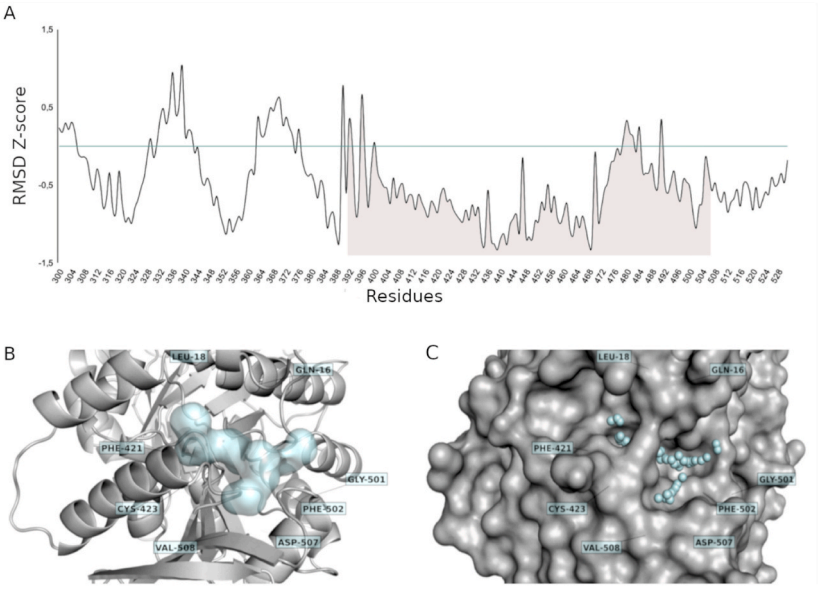

Fig. 4. Identification of the druggable pocket within the dimer-dimer interface. (A). Graphical representation of the Z-score calculated for the region encompassing residues 300–506 of PKM2. The shaded grey area includes residues from the Cα1 and Cα2 helices and most residues within the identified druggable pocket. (B). The image illustrates the druggable pocket at the dimer-dimer interface of PKM2, with a ribbon representation of the protein and the pocket volume depicted as a light green surface. (C). The pocket is shown with the protein surface in grey, highlighting the druggable pocket with light green spheres. The labelled residues within the pocket are encoded by exon 10 of PKM2.

values lower than −9.5 kcal/mol (Table 1). This result was combined with visual analysis of the poses of the top-ranked predicted ligands by Autodock Vina.

The selection criteria were defined by the highest negative binding affinities and the presence of multiple atom-residue contacts, emphasising those that establish hydrogen bonds and multiple hydrophobic interactions, ensuring a thorough evaluation. The analysis of the non-covalent interactions was performed using a widely used tool for the visualisation and identification of relevant non-covalent protein–candidate contacts, the Schrodinger Maestro software. The analysis showed that the dominant interactions for the compounds are hydrophobic, with only three candidates forming hydrogen bonds. Specifically, Arg447 and Phe421 establish hydrogen bonds and π-cation or π-stacking interactions, respectively. Additionally, all the compounds interact with the residue Cys424, determining the different catalytic and modulatory properties between PKM splicing isoforms [53].

3.3. Chemical diversity of top-ranked candidates identified through DBVS analysis

The Tanimoto Coefficient of Similarity was calculated using two fingerprints methods to ensure the chemical diversity of the top ten candidates: Morgan (radius 2, 1024 bits) and MACCS (166 bits) 2D fingerprints [54]. This analysis involved pairwise comparisons among the top ten compounds identified by the DBVS (Fig. 5).

The Morgan 2D fingerprint, commonly used in structure-activity models, fragments molecules into circular atom neighbourhoods, generating variable-length fingerprints. The highest similarity scores using the Morgan fingerprint were found between compound C599 and C523, with a score of 0.67, and between C116 and C599, with a score of 0.69. Additionally, C986 and C828 showed a similarity score of 0.66. All other compounds had a similarity coefficient below 0.55, indicating substantial chemical diversity, as none exceeded the threshold of 0.85, which is typically used to identify structurally similar compounds.

For further analysis, the MACCS keys, comprising 166 predefined structural patterns relevant to drug discovery, were used to evaluate chemical similarity. The MACCS-based analysis revealed score values above the 0.85 threshold for C523 in comparison with C116 and C599, and for C561 in comparison with C188. For all other compounds, the similarity scores were below 0.85, confirming that the ligands possess diverse chemical motifs, though none scored below 0.5, reflecting their common drug-like properties. Based on these analyses, we selected and acquired ten molecules from Enamine (Table 1).

3.4. Experimental evaluation of candidates

3.4.1. In vitro cell proliferation assay of top-ranked candidates in glioblastoma cell lines

Glioblastoma multiforme (GBM) is an extremely aggressive tumour, characterised by poor survival rates despite aggressive treatments [55]. The overexpression of PKM2, coupled with reduced PKM1 levels in GBM compared to normal brain tissue, contributes to the malignant phenotype through both its glycolytic and non-canonical activities [56,57].

Given this, we selected the high-grade malignant glioma cell lines LN299, U87, and U251 to assess whether the identified candidate compounds could inhibit cell proliferation and to determine their IC_{50} values. These cell lines exhibit higher PKM2 protein expression levels compared to other tumour-derived cell lines or normal brain tissue [57,58].

The cell lines were treated with the selected compounds from Enamine at concentrations ranging from 12.5 to 100 μM for 48h, and cell viability was evaluated using the MTS assay. As shown in Table 2, both C599 and C998 significantly reduced cell growth and viability in a dose-dependent manner, with IC_{50} values in the micromolar range. Notably, C998 exhibited lower IC_{50} values, indicating a stronger effect on growth inhibition across all three cell lines.

The remaining candidates showed IC_{50} values above 100 μM (data not shown). Since the U87 glioblastoma cell line displayed the highest sensitivity to the compounds and possessed greater migration and invasion capabilities [59], it was chosen for further *in vitro* assays.

3.4.2. Evaluation of apoptotic induction and pyruvate kinase activity inhibition by selected top-ranked candidates C599 and C998

Caspase 3/7 activity was analysed using the Caspase-Glo® 3/7 Assay System to assess apoptosis activity *in vitro*, as described in the Experimental Section. As shown in Fig. 6A–a 24h treatment with both compounds, at concentrations similar to their respective IC_{50} values, resulted in a significant increase in caspase 3/7 activity in treated U87 cells compared to the control. The results indicate

Table 1
Molecular interaction profile of candidates with H-bonds **highlighted**. HI: Hydrophobic interaction, HB: Hydrogen bond, pS: π-stack, pCat: π-cation.

Compound	ΔG (kcal/mol)	Interaction type	Residues involved
C523	−10.1	8HI-1pS-2 pC	18,40,42,392,395,418,421,424,447,448,449,502
C561	−10.0	8HI-**2HB**-1pS	18,22,392,395,418,421,422,424,424,446,448,**447**
C599	−9.9	9HI-1pS-1 pC	18,40,392,395,418,421,424,447,448,449,502
C986	−9.9	8HI-1pS-1 pC	18,40, 392,395,418,421,424,447,448,449
C828	−9.8	9HI-1pS-1 pC	18,40,392,395,418, 421,424,447,448,449,502
C118	−9.8	11HI, 1 pS, 1 pC	18,22,40,42,392,395,418,421,424,448,449,502,
C632	−9.8	8HI-1pS	21,40, 392,395,418,421,424,448,502
C998	−9.7	11HI-1pS	18, 21,22,40,42,392,421,424,448,449,502
C116	−9.7	8HI-**1HB**-1pS-1 pC	**16**, 40,392,395,418,421,424,447,448,449,502
C710	−9.7	8HI, **1HB**,1 pS	18,21,22,392,395,418,421,424, **447**,448

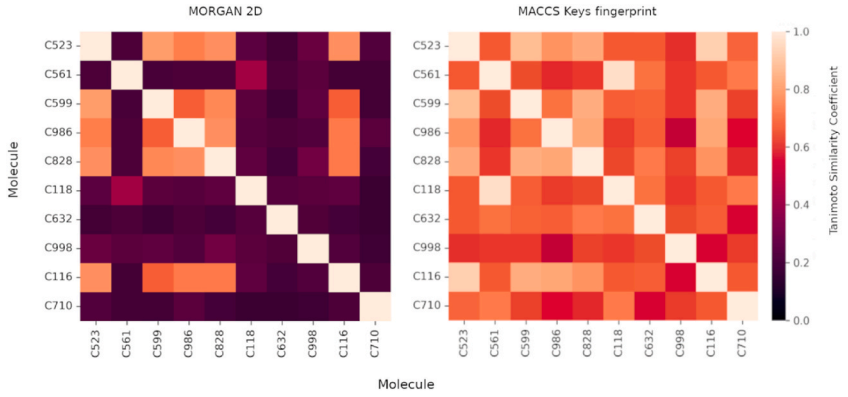

Fig. 5. Chemical diversity of the compounds. The matrices show the similarity among the top 10 compounds based on the Tanimoto Coefficient of Similarity (1 indicates identity) using Morgan and MACCS 2D fingerprints.

Table 2
Antiproliferative activity compounds on different glioma cell lines. Results are expressed as the concentration required to induce 50 % inhibition of cell proliferation (IC_{50}) and the maximal inhibition achieved following 48h exposure to candidates. Data are presented as means and corresponding 95 % confidence intervals (CI_{95}) (n = 3).

Compound	IC50 μM (CI_{95})		
	LN299	U87	U251
C599	56,68 (48,4-89,4)	49,67 (31,2-32,6)	37,61 (34,0-42,3)
C998	28,49 (23,17-36,3)	13,61 (12,4-15,0)	22,09 (10,3-14,7)

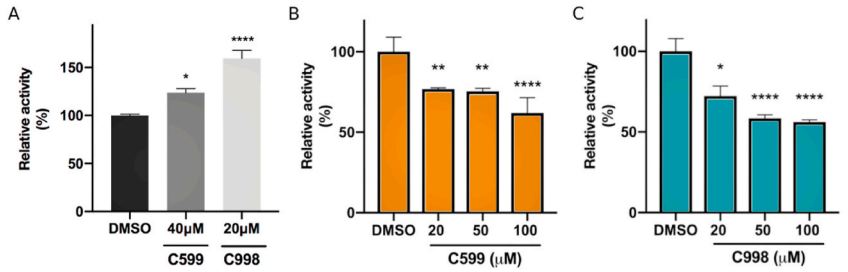

Fig. 6. (A). Apoptosis as determined with a caspase 3/7 activity assay after treatment with C599 and C998 compounds in U87 cell line (B). Pharmacological inhibition of PKM2 enzymatic activity. PK activity in the presence of different concentrations of C599 and C998 with U87 cell line (n = 3). Data were normalised to DMSO-treated PK activity. Mean ± SD, *p ≤ 0.05; **p ≤ 0.01; ***p ≤ 0.001; ****p ≤ 0.0001.

significant apoptosis induction for both compounds. Compound C998 exhibited a greater apoptotic effect (59 %) compared to C599 (23 %) at concentrations of 20 μM and 40 μM respectively, suggesting that the compounds' effects on proliferation are mediated by an apoptosis-driven mechanism. Altogether, these results confirm the *in vitro* anticancer potential of both compounds.

To evaluate the impact of C599 and C998 on pyruvate kinase (PK) activity, we assessed their effects on human glioblastoma U87 cells. As illustrated in Fig. 6B and C, 2h treatment with both compounds led to a significant, dose-dependent reduction in PK activity compared to the DMSO-treated control. At a concentration of 20 μM, both compounds reduced PKM2 activity by approximately 30 %, with maximum inhibition observed at 50 μM for C998 (58 %) and at 100 μM for C599 (61 %). Considering that the tetrameric form of PKM2 displays the highest enzymatic activity [60], these findings suggest that both small molecules can disrupt full PKM2 activation *in vitro*.

3.4.3. Evaluation of pharmacokinetic profile using ADMET analysis

Drug discovery programmes often fail during clinical trials due to toxicity, lack of efficacy, or unacceptable side effects. Defining the pharmacokinetic profile early in drug development maximises a compound's therapeutic potential [61].

Regarding drug-like properties, we conducted virtual screening using the publicly available Enamine Advanced Collection, which contains over 500,000 drug-like compounds that already adhere to the Lipinski Rule of Five (RO5), ensuring that the selected compounds possess these essential properties.

Further pharmacokinetic properties, including ADME and toxicity parameters (ADMET), of the top 10 ranked molecules were

evaluated using the pkCSM prediction tool [33] (Supplementary Table S1). The active compounds, C599 and C998, were highlighted, and their results are presented below.

Human intestinal absorption (%HIA) and the Caco-2 cell line assay model were used to predict the absorption of orally administered compounds. Both candidates showed HIA values above 90 % and acceptable pCaco values. Regarding predicted metabolic reactions, only C998 is anticipated to be a CYP2D6 substrate, although neither compound is predicted to inhibit Cytochrome P450 enzymes. Since our screening focuses on targeting tumours in the central nervous system (CNS), we evaluated whether the compounds have CNS permeability. Both candidates demonstrated CNS permeability, as measured by the blood-brain permeability surface area product. Additionally, both C599 and C998 were negative in the Ames test, indicating a lack of mutagenic potential.

Finally, while neither candidate showed toxicity as an hERG I inhibitor, C998 is predicted to potentially inhibit hERG II.

In conclusion, the ADMET properties analysed by pkCSM suggest that both identified molecules meet the drug-likeness criteria, making them suitable candidates for the design of potential PKM2 inhibitors.

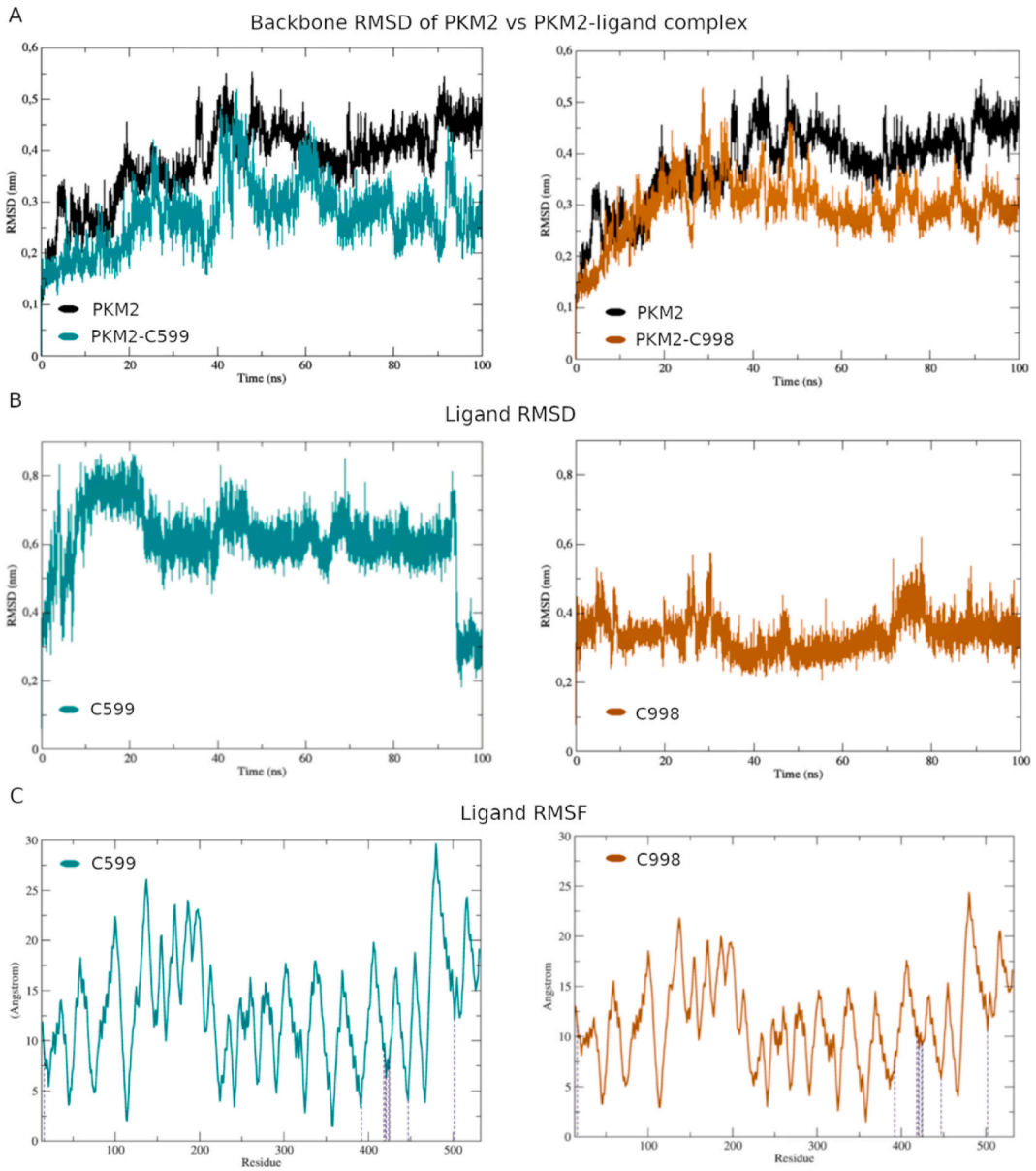

Fig. 7. (A). Root-mean-square deviation (RMSD) (B). Free PKM2 (black) and PKM2 in complex with C599 (turquoise) and C998 (orange) as a function of time. (C) Root-mean-square fluctuation (RMSF) of PKM2 in complex with C599 (turquoise) and C998 (orange).

3.5. Molecular dynamics simulations: evaluating the structural stability of PKM2-Ligand complexes

3.5.1. RMSD, RMSF and Rg analysis of PKM2 complexes

To evaluate the stability of the interactions between PKM2 and the ligands C599 and C998, we analysed key parameters derived from the MD simulations, including RMSD, RMSF, and Rg [62].

The root mean square deviation (RMSD) is a crucial metric for assessing the global flexibility of a protein, with lower RMSD values reflecting reduced mobility and indicating enhanced system stability. Following the equilibration steps (Supplementary Figs. S3, S4, and S5), the RMSD of free PKM2 and its complexes with C599 and C998 were monitored over 100 ns to evaluate the stability of the complexes relative to the unbound protein (Fig. 7A). Both complexes demonstrated lower RMSD values compared to free PKM2. Specifically, the PKM2-C998 complex stabilised at 14.9 ns and maintained an average RMSD of 0.3 nm for the remainder of the simulation. In contrast, the PKM2-C599 complex exhibited higher initial fluctuations before reaching a stable state. These results suggest that the observed RMSD values correspond to equilibrium states for both complexes, consistent with the notion that minimal RMSD fluctuations are indicative of system stability [63].

The RMSD of ligands C599 and C998 were analysed to gain further insight into the protein-ligand interactions after backbone least-squares fitting (Fig. 7B). C998 displayed remarkable stability throughout the 100 ns simulation, with an average deviation of 0.33 nm from its initial position. Conversely, C599 experienced an initial spike in RMSD, peaking at 0.8 nm before stabilising within the range of 0.4–0.6 nm. Notably, at around 90 ns, C599 reverted to its original conformation, suggesting the presence of two distinct conformational states during the simulation.

Additionally, the root mean square fluctuation (RMSF) analysis was conducted to examine residue-specific flexibility, focusing on PKM2 residues interacting with the ligands (Gln16, Leu392, Glu418, Ser420, Phe421, Cys424, Ser425, Arg447, Phe502). The results revealed that the mobility of these residues was not significantly altered by the presence of C599 or C998, largely because the majority of interacting residues exhibited inherently low flexibility (Fig. 7C).

The radius of gyration (Rg) (Supplementary Fig. S3, S4 and S5) was used to evaluate the overall structural compactness and stability of the protein-ligand complexes. The Rg values for the PKM2 complexes with C599 and C998 remained stable throughout the 100

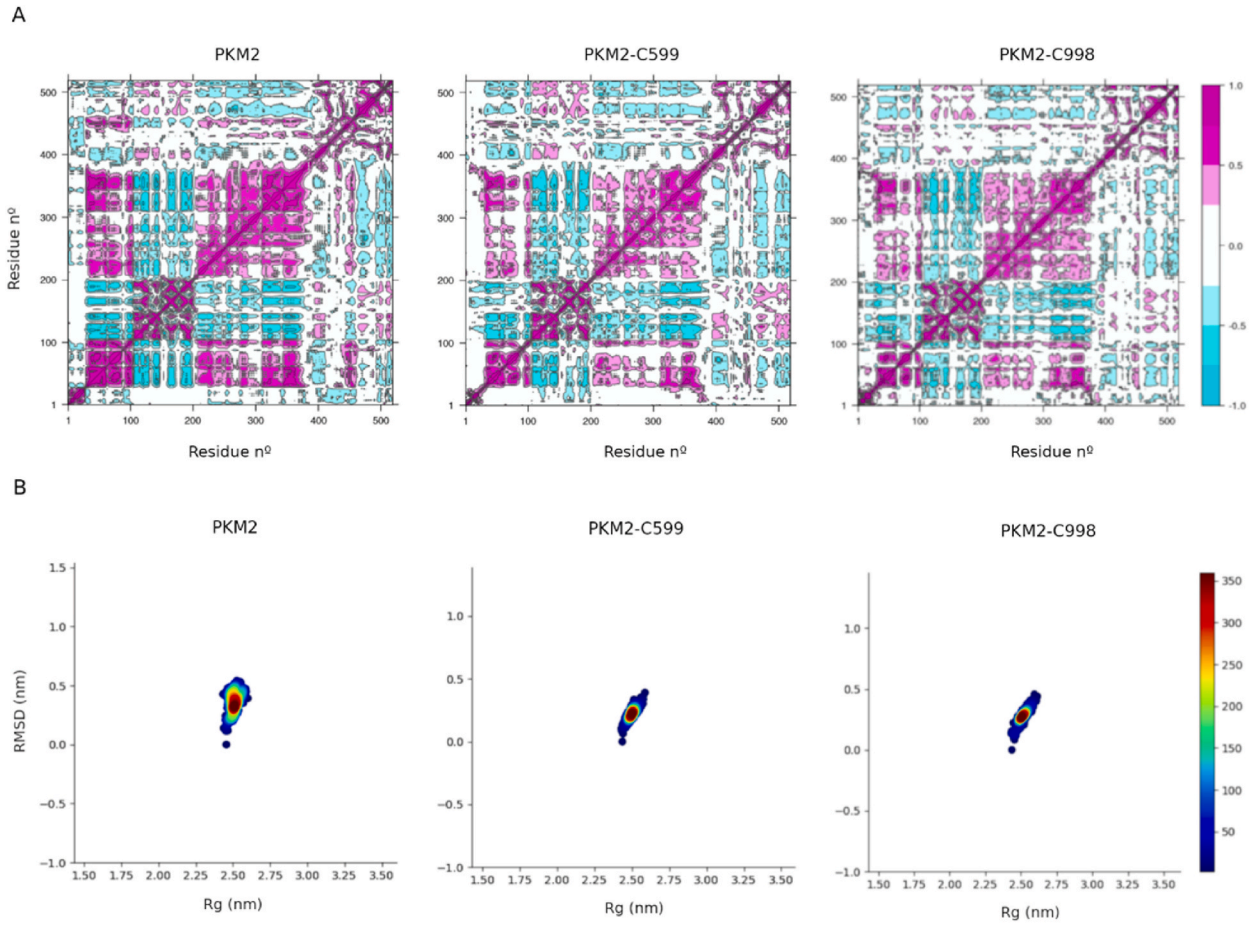

Fig. 8. (A). Dynamic cross correlation matrix (DCCM) and (B) Probability density function (PDF) analysis for free PKM2 and PKM2 in complex with compounds C599 and C998.

ns trajectory, reflecting robust protein-ligand interactions. Furthermore, the comparison of Rg values between the free protein and the complexes revealed no substantial changes, indicating that neither ligand induced abrupt conformational rearrangements in the protein structure.

3.5.2. Dynamic cross-correlation and probability density function analyses reveal stabilising effects of ligand binding on protein motion

The DCCM for each of the simulations was performed by aligning the trajectory to the starting frame to remove overall translational and rotational motions. The fitted trajectory data were then used to compute the DCCM, which quantifies the correlated motions of atomic pairs during the simulation. As shown in Fig. 8A, the DCCM results exhibit the same trend across all three simulations, with protein regions that correlate and anti-correlate remaining unaffected by the presence or absence of the ligands. However, there is a clear decrease in the magnitude of correlation and anti-correlation in the movements of different protein regions in the presence of the ligands. This suggests that, while the interaction with the ligands does not alter the correlated movements of the protein, it impacts the intensity of these motions, most likely due to a stabilising effect of the ligand-protein interaction.

When constructed using the radius of gyration (RG) and RMSD, the kernel density estimate-dependent PDF analysis shows the likelihood of a given state being sampled in an MD simulation trajectory.

As expected, given the previous results, the PDF analysis of both PKM2 in complex with C599 and C998 shows a slightly more concentrated distribution regarding the conformational population compared to that of free PKM2 (Fig. 8B). All three simulations show similar values for the RG: 2.51 nm for free PKM2 and 2.50 nm for PKM2 in complex with C599 and C998 at the most populated

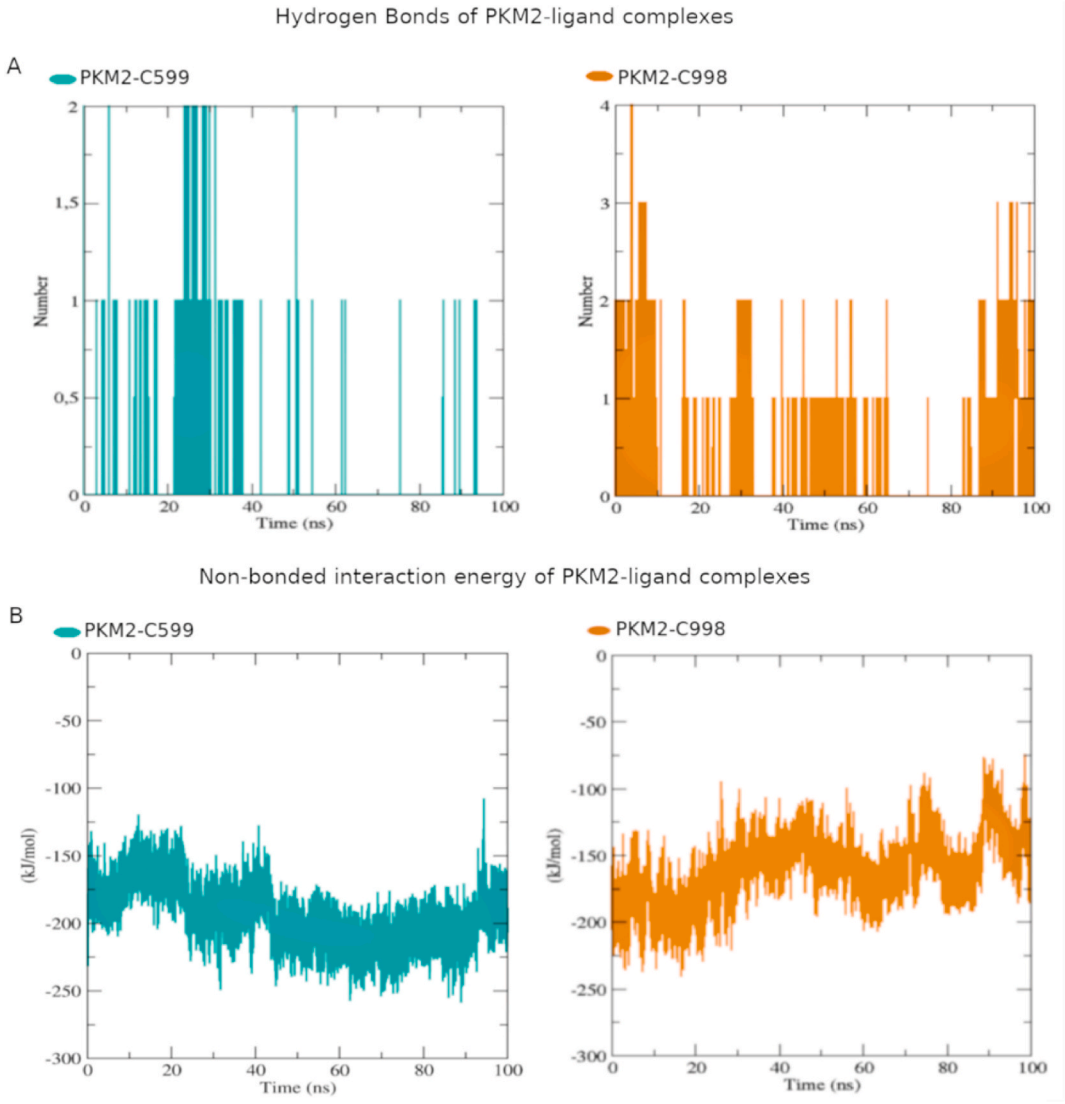

Fig. 9. (A) The number of Hydrogen bonds formed in the PKM2-C4 complex concerning simulation time throughout the trajectory. (B) Non-bonded interactions within the protein-ligand complex throughout the trajectory.

conformation. On the other hand, the PDF for free PKM2 shows a higher RMSD value at 0.32 nm, while PKM2-C599 and PKM2-C998 show values of 0.22 nm and 0.27 nm, respectively.

3.5.3. *Hydrogen bond analysis in MD trajectories*

To further investigate the stability of the protein-ligand interactions, we conducted a detailed analysis of hydrogen bonds formed between PKM2 and the ligands C599 and C998 throughout the molecular dynamics simulations. Hydrogen bonds are crucial in

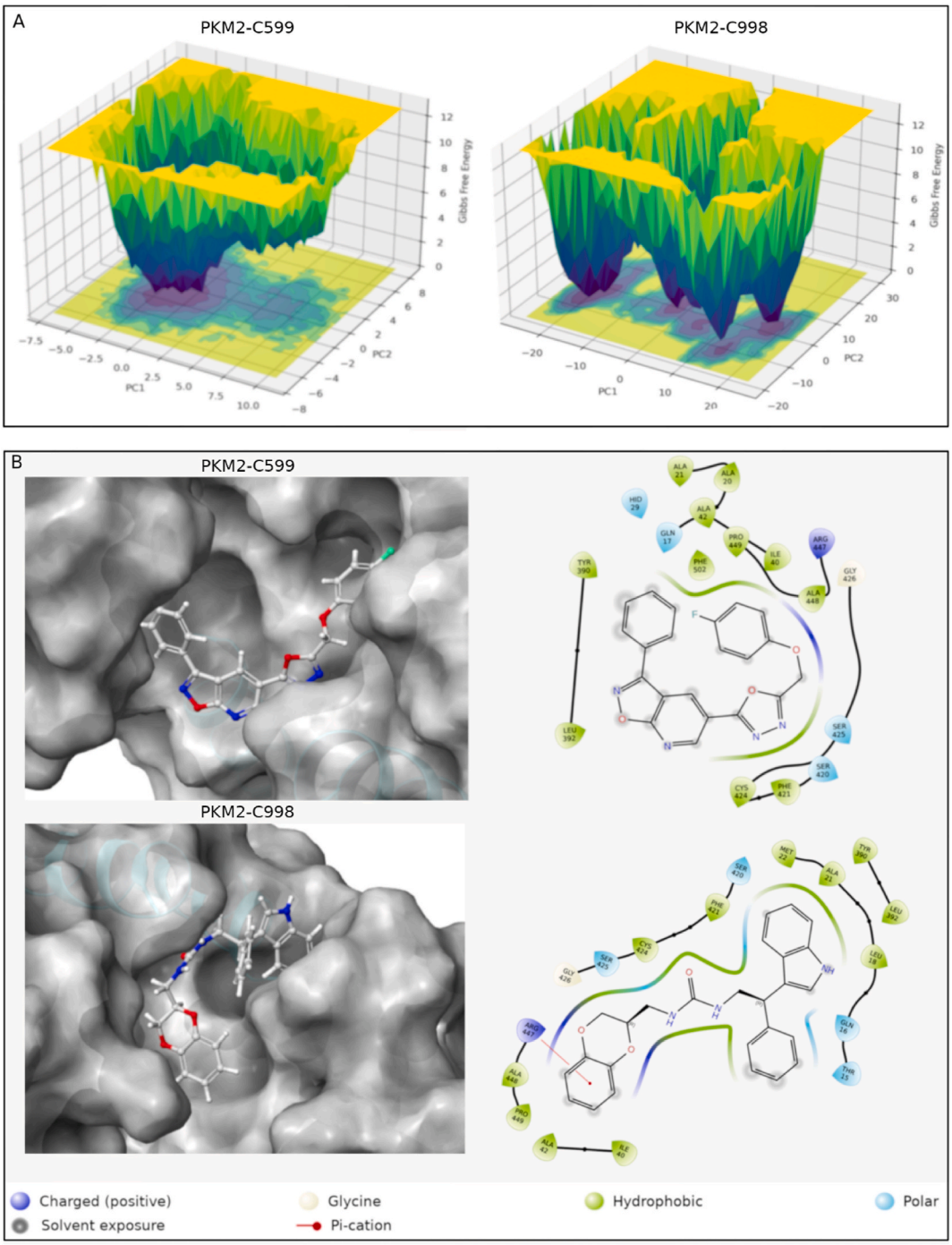

Fig. 10. (A). 3D Gibbs free energy landscapes (FEL) of PKM2-C599 and PKM2-C998 complexes as function of projections of the MD trajectory onto PC1 and PC2 eigenvectors, (B). 2D Diagram with close contact interactions of C599 and C998 with the binding pocket. (C). 3D Surface representation of PKM2-C599 and PKM2-C998 complexes.

stabilising protein-ligand complexes, and their presence indicates strong interactions that can contribute to the system's overall stability.

Our analysis revealed that C599 and C998 maintained a consistent hydrogen bonding pattern with PKM2 during the 100 ns trajectory. Specifically, the average number of hydrogen bonds formed by C998 was observed to be higher than that of C599, suggesting a stronger and more stable interaction (Fig. 9). Notably, ligand C998 formed between two and four hydrogen bonds, whereas C599 formed one to two hydrogen bonds.

Furthermore, the interactions between PKM2 and the ligands were corroborated by analysing the short-range Coulomb (Coul-SR) and short-range Lennard-Jones (LJ-SR) energy terms. The total interaction energy of the complexes exhibited negative values for both complexes, indicating that both ligands formed thermodynamically stable bonds. The total averages for C599 and C998 were -194.92 ± 21.83 kJ/mol and -161.58 ± 25.10 kJ/mol, respectively (Fig. 9). In this case, C599 presented a more stable interaction with more negative values than the C998 profile.

The observed energy profile underscores the significant role of non-bonded interactions in maintaining the structural integrity and stability of the complexes. Overall, these results highlight that the protein-ligand interactions remain stable throughout the simulation, emphasising the potential of these ligands as viable candidates for further development.

3.5.4. Free energy landscapes and interaction analysis of PKM2-Ligand complexes

The covariance matrix of a simulation describes the correlation between all motions of the system's atoms throughout the entire trajectory. From this extremely complex and high-dimensional dataset, the maximum variance of the atomic positions was obtained through Principal Component Analysis (PCA). PCA involves the calculation of the eigenvectors and eigenvalues of the diagonalised covariance matrix, which provide the direction of the principal components and their significance.

The first two principal components (PCA1, PCA2) capture the most significant motions of the protein. To determine the free energy landscape (FEL) of the protein, the trajectory of the simulation is projected onto PCA1 and PCA2. The FEL represents the stability and accessibility of different conformational states of the system, with low-energy basins indicating more stable conformations [64].

Fig. 10A shows the Free Energy Landscape (FEL) of the PKM2-C599 and PKM2-C998 complexes, where the dark purple indicates the most stable conformation. Global energy minimum frame was selected as the most stable structure for further analysis. As shown in Fig. 10B, both C599 and C998 establish hydrophobic interactions with Leu392, Phe421, Cys424, and polar contacts with Ser420, Ser425, and Arg447 of PKM2. Notably, PKM2 residues such as Leu392, Phe421, Cys424, Ser425, and Gly426 are replaced in the M1 isoform by Arg, Tyr, Leu, Ala, and Ala, respectively. Cys424 plays a crucial role in stabilising PKM2's R-state, with its protonation regulating the enzyme's allosteric transition [59,60]. The interaction of both inhibitors with these residues, especially Cys424, suggests that they may interfere with the active tetrameric form of PKM2, offering selectivity over the M1 isoform. While both candidates interact with the positively charged Arg447, C998 forms a stronger π-cation interaction. Arg447 is involved in CARM1-mediated methylation, which promotes the formation of the active tetramer through stabilising interactions with Leu392 and Phe421 [65]. Mutations in these residues impair PKM2 regulation, indicating that these compounds target a key region for post-translational control. Additionally, the C998 complex at the energy minimum shows two water-mediated hydrogen bonds, further stabilising the interaction.

Fig. 10C presents a 3D representation of the druggable pocket with the ligand positioned within it, illustrating the pocket's surface. This visual highlight the spatial arrangement of C599 and C998 within the pocket.

3.5.5. Evaluating the interaction strength of ligands with PKM2 through steered molecular dynamics

Steered Molecular Dynamics has recently emerged as an effective, yet computationally inexpensive technique to assess the strength of the interaction between a ligand and a protein. Multiple SMDs were performed to ascertain the rupture force of the unbinding of C599 and C998 from PKM2 using the global energy minima identified previously as the starting position of the simulations (Table 3).

The average rupture forces for C599 and C998 were 969.33 ± 80.17 and 917.83 pN ± 63.25, respectively, comparable to known high-affinity binders in other systems [46]. This rupture force can serve as a proxy for the binding affinity, as a higher rupture force typically correlates with stronger ligand-protein interactions, suggesting a more stable complex. To illustrate the ligand unbinding process observed during the simulation, Fig. 11A and B presents representative plots of both the pulling force and the centre-of-mass (COM) distance between each ligand and PKM2 throughout the SMD simulation. At the beginning of the simulation, the force exerted by the virtual spring is insufficient to overcome the high-affinity interactions between the ligand and the PKM2 binding pocket, resulting in a stable COM distance. As the pulling force gradually increases, it eventually reaches a critical point, known as the rupture force, where the ligand is released from the binding site. At this moment, the COM distance increases as the ligand moves along the reaction coordinate, signifying its unbinding from PKM2. This analysis demonstrates the utility of SMD in predicting the quality of

Table 3
The table shows the individual rupture force of each SMD simulation and the corresponding distance at which it occurred for C599 and C998.

SMD	C599		C998	
	Rupture Force (pN)	Distance (nm)	Rupture Force (pN)	Distance (nm)
SMD 1	904.29	2.48	842.39	2.69
SMD 2	1037.26	2.48	864.42	2.73
SMD 3	1048.91	2.52	931.67	2.89
SMD 4	845.76	2.52	1023.58	2.77
SMD 5	1010.42	2.47	927.09	2.70

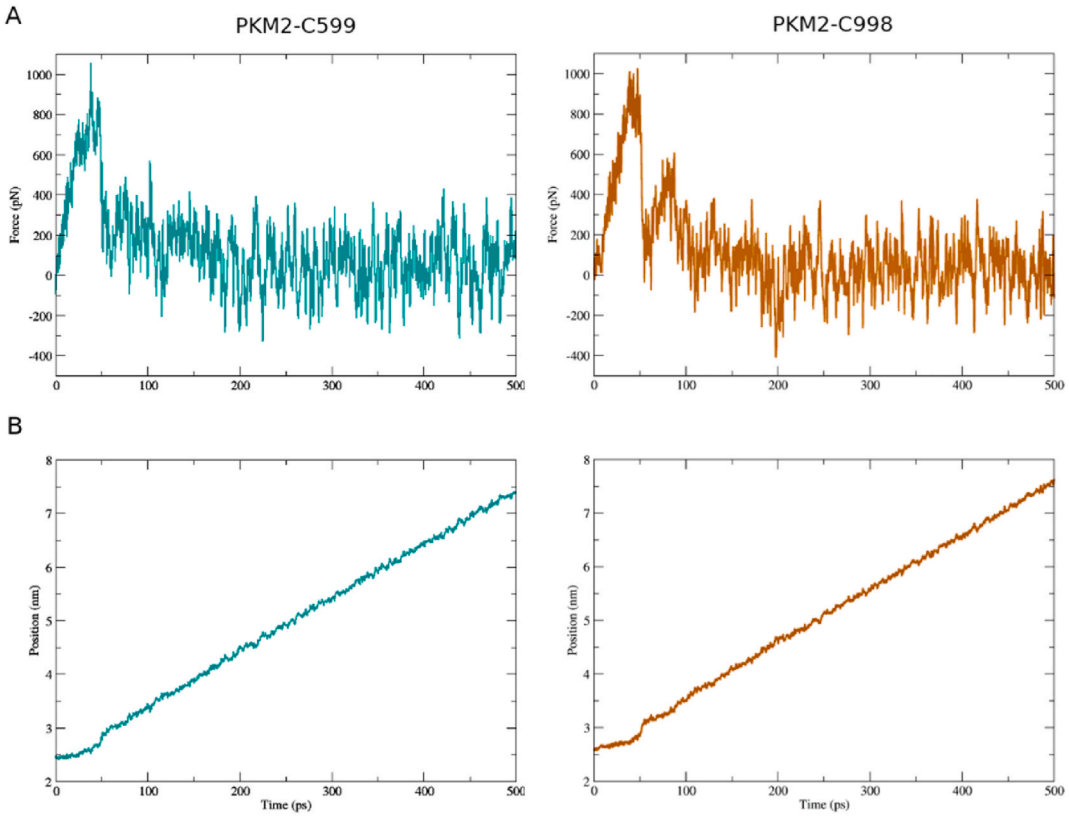

Fig. 11. (A). Representative plots of the pulling force between each ligand and PKM2 throughout the SMD simulation. (B). Representative plots of the centre-of-mass (distance).

protein-ligand interactions and correlates well with binding affinity constants, providing valuable insights for future drug design.

4. Discussion

PKM2 is a prime example of a multifunctional metabolic enzyme, with its highly interdependent conformational states (tetramer, dimer, monomer), subcellular localisation (cytoplasm, nucleus), and biological activity. As a morpheein, PKM2 presents an opportunity for designing small molecules that can stabilise and shift their conformation towards a specific state, providing a novel approach for PKM2 inhibitor design. In this study, we identified and characterised a novel druggable pocket at the dimer–dimer interface of the PKM2 isoform, a promising therapeutic target in glioblastoma. Glioblastoma is an aggressive malignancy in which PKM2 is overexpressed, and inhibiting its activity has been associated with inducing apoptosis in glioma cells [13,49].

The literature has described only two PKM2 inhibitors with demonstrated anti-tumour activity in glioblastoma models: Shikonin [19,66] and Gliotoxin [20], both naturally occurring compounds. The treatment of glioblastoma brain tumours using Shikonin has shown promise in preclinical studies, but there is limited data on the ability of Shikonin to cross the blood-brain barrier (BBB). It also has off-target effects on normal, healthy cells, raising concerns about toxicity [67]. The other inhibitor gliotoxin induces cell death in glioblastoma cells coupled with inhibition of PKM2, although its toxicity limits therapeutic use without further modification [68]. As Zahra et al. highlighted in their elegant work, "further studies are required in order to make PKM2 a fruitful target for cancer therapy" [69].

The identification of newly designed PKM2 inhibitors, as demonstrated in this work, offers a promising avenue for the future of glioblastoma treatment. This study's novelty lies in identifying new PKM2 inhibitor candidates through a docking-based virtual screening approach, specifically targeting a recently characterised druggable pocket located at the C-C′ interface of PKM2. We achieved this discovery by integrating bioinformatics, structural, and biological approaches.

In this study, two compounds were identified that exhibited antiproliferative activity and cellular activation of caspase 3/7 in a panel of glioblastoma cell lines. These results indicate a pro-apoptotic activity of the compounds suggesting the *in vitro* anticancer potential. Furthermore, the direct inhibition of PKM2 enzymatic activity suggests the molecular mechanism of action of the proposed candidates, experimentally confirming the rationale behind the design.

An important consideration in the design of compounds with potential antitumoural activity is the analysis of off-target effects, and, particularly for GBM, the prediction of CNS permeability. Our analysis showed that both candidates exhibited acceptable ADME and

toxicity parameters. Additionally, both are predicted to be CNS permeable, demonstrating their great potential as novel PKM2 inhibitors for the treatment of GBM.

Finally, through MD simulations, we confirmed that both candidates had established thermodynamically favourable interactions within the identified binding pocket. Additional analysis of the pocket highlighted critical residues responsible for CARM-1 post-translational control and R-state stabilization, both associated with full enzyme activity. The interaction of both inhibitor candidates with these residues, particularly Cys424, suggests that these compounds may interfere with the formation of the fully active tetrameric form of PKM2, indicating selectivity over the M1 isoform. However, whether these compounds induce a low-affinity T-state or directly disrupt tetramer formation remains to be determined. Further investigation is necessary to fully elucidate their precise mechanisms of action. In addition, our SMD analysis revealed rupture forces consistent with those observed for high-affinity binders, supporting the *in vitro* results and reinforcing the potential of these compounds as effective PKM2 inhibitors. Our findings demonstrate the value of combining structural analyses with computational modelling to predict protein-ligand interactions.

This integrated approach, combining detailed structural analysis, DBVS, molecular dynamics simulations and biological evaluation, enabled the identification of novel compounds capable of modulating PKM2 activity, ultimately demonstrating antitumor activity against human glioblastoma models.

5. Conclusions

In this study, we identified and characterized a novel druggable pocket at the dimer–dimer interface of the PKM2 isoform, a promising therapeutic target in glioblastoma. By screening over 500,000 drug-like compounds, we selected ten molecules that showed robust interactions with this pocket. Among these, C599 and C998 stand out for their significant antiproliferative activity in glioblastoma cell lines with IC_{50} values in the micromolar range.

Experimental assays in glioblastoma cells confirmed that C599 and C998 significantly inhibit PKM2 enzyme activity, showing a dose-dependent effect. Furthermore, these compounds induced apoptosis in glioblastoma cells, as evidenced by the activation of caspases 3 and 7, further supporting their potential as therapeutic agents.

Molecular dynamics (MD) simulations revealed stable, high-affinity interactions between PKM2 and both compounds, confirmed by Steered Molecular Dynamics (SMD) simulations, which showed rupture forces comparable to those of high-affinity inhibitors in other systems. These interactions involved key residues at the dimer–dimer interface, suggesting that both compounds effectively alter the oligomeric state of PKM2.

In summary, these candidates may serve as lead compounds, providing a foundation for the design of novel analogues with improved activity and translational potential. Our findings demonstrate the value of combining structural analyses with computational modelling to predict protein-ligand interactions. This approach accelerates the early stages of drug discovery and increases the confidence in identifying promising therapeutic candidates. However, additional research is imperative to refine our understanding of the compounds' mechanisms and optimise their therapeutic potential, highlighting the importance of our work in advancing glioblastoma treatment.

CRediT authorship contribution statement

Maia Cabrera: Writing – review & editing, Writing – original draft, Validation, Methodology, Investigation, Funding acquisition, Data curation, Conceptualization. **Romina Armando:** Writing – review & editing, Validation, Methodology, Investigation, Formal analysis, Data curation. **Ian Czarnowski:** Writing – review & editing, Investigation, Conceptualization. **Patricio Chinestrad:** Writing – review & editing, Software, Methodology, Investigation, Formal analysis. **Ramiro Blanco:** Writing – review & editing, Software, Formal analysis. **Alejandra Zinni:** Writing – review & editing, Investigation, Funding acquisition, Formal analysis, Data curation. **Daniel Gómez:** Writing – review & editing, Validation, Investigation. **Diego L. Mengual Gómez:** Writing – review & editing, Methodology, Investigation, Data curation. **Pablo Lorenzano Menna:** Writing – review & editing, Supervision, Resources, Project administration, Funding acquisition, Conceptualization.

Data availability statement

Data included in article/supplementary material/referenced in article.

Ethics approval and consent to participate

Not applicable.

Consent for publication

Not applicable.

Declaration of generative AI and AI-assisted technologies in the writing process

During the preparation of this work, the authors Cabrera Maia and Lorenzano Menna Pablo used ChatGTP to improve the

readability and language of the manuscript. After using this tool, both authors reviewed and edited the content as needed and takes full responsibility for the content of the publication.

Funding

The present study was supported by grants from: Agencia Nacional de Promoción Científica y Tecnológica (ANPCYT) PICT number 2625 PI: Lorenzano Menna Pablo. Agencia Nacional de Promoción Científica y Tecnológica (ANPCYT) PICT number 97/2021 PI: Cabrera Maia. Universidad Nacional de Quilmes: Grant number: 2297/22 PI: Zinni Maria Alejandra.

Declaration of competing interest

The authors declare that they have no known competing financial interests or personal relationships that could have appeared to influence the work reported in this paper.

Abbreviations

ADMET	absorption distribution metabolism excretion and toxicity
BSA	buried surface area
CAAD	computer-aided drug design
CNS	Central nervous system
COM	centre-of-mass
DBVS	docking-based virtual screening
DMEM	Dulbecco's modified Eagle's medium
DMSO	Dimethyl sulfoxide
FBP	fructose bisphosphate
FEL	Free Energy Landscape
GBM	Glioblastoma multiforme
GLUTs	glucose transporters
HIA	Human intestinal absorption
MACCS	Molecular Access System
MD	Molecular Dynamic
ORCT	Oral rat chronic toxicity
PDB	Protein Data Bank
PCA	principal component analysis
PCs	Principal Components
PKM2	pyruvate kinase isoform M2
PMTS	post-translational modifications
PPP	pentose phosphate pathway
RMSD	Root Mean Square Deviation
RMSF	Root Mean Square fluctuation
ROS	reactive oxygen species
SAICAR	Succinyl amino imidazole carboxyamide ribose-5-phosphate
SD	standard deviation
SMD	steered molecular dynamics
ps	picoseconds

Appendix A. Supplementary data

Supplementary data to this article can be found online at https://doi.org/10.1016/j.heliyon.2025.e42238.

References

[1] E.K. Jaffe, Impact of quaternary structure dynamics on allosteric drug discovery, Curr. Top. Med. Chem. 13 (1) (2013) 55–63.
[2] S.H. Lawrence, E.K. Jaffe, Expanding the concepts in protein structure-function relationships and enzyme kinetics: teaching using morpheeins, Biochem. Mol. Biol. Educ. 36 (4) (2008) 274–283.
[3] E.K. Jaffe, Morpheeins–a new structural paradigm for allosteric regulation, Trends Biochem. Sci. 30 (9) (2005 Sep) 490–497.
[4] F.V. Filipp, Cancer metabolism meets systems biology: pyruvate kinase isoform PKM2 is a metabolic master regulator, J. Carcinog. 12 (2013 Jul 24) 14.
[5] S. Mazurek, Pyruvate kinase type M2: a key regulator of the metabolic budget system in tumor cells, Int. J. Biochem. Cell Biol. 43 (7) (2011 Jul) 969–980.
[6] J.D. Dombrauckas, B.D. Santarsiero, A.D. Mesecar, Structural basis for tumor pyruvate kinase M2 allosteric regulation and catalysis, Biochemistry 44 (27) (2005 Jul 12) 9417–9429.

[7] T. Hitosugi, S. Kang, M.G. Vander Heiden, T.-W. Chung, S. Elf, K. Lythgoe, et al., Tyrosine phosphorylation inhibits PKM2 to promote the Warburg effect and tumor growth, Sci. Signal. 2 (97) (2009 Nov 17) ra73.
[8] S. Mazurek, Pyruvate kinase type M2: a key regulator within the tumour metabolome and a tool for metabolic profiling of tumours, Ernst Schering Found Symp Proc. (4) (2007) 99–124.
[9] S. Mazurek, C.B. Boschek, F. Hugo, E. Eigenbrodt, Pyruvate kinase type M2 and its role in tumor growth and spreading, Semin. Cancer Biol. 15 (4) (2005 Aug) 300–308.
[10] B. Rathod, S. Chak, S. Patel, A. Shard, Tumor pyruvate kinase M2 modulators: a comprehensive account of activators and inhibitors as anticancer agents, RSC Med. Chem. 12 (7) (2021 Jul 21) 1121–1141.
[11] P. Chen, L. Lou, B. Sharma, M. Li, C. Xie, F. Yang, et al., Recent advances on PKM2 inhibitors and activators in cancer applications, Curr. Med. Chem. 31 (20) (2024) 2955–2973.
[12] J. Li, S. Li, J. Guo, Q. Li, J. Long, C. Ma, et al., Natural product micheliolide (MCL) irreversibly activates pyruvate kinase M2 and suppresses leukemia, J. Med. Chem. 61 (9) (2018 May 10) 4155–4164.
[13] K. Rock, O. McArdle, P. Forde, M. Dunne, D. Fitzpatrick, B. O'Neill, et al., A clinical review of treatment outcomes in glioblastoma multiforme–the validation in a non-trial population of the results of a randomised Phase III clinical trial: has a more radical approach improved survival? Br. J. Radiol. 85 (1017) (2012 Sep) e729–e733.
[14] J.P. Thakkar, T.A. Dolecek, C. Horbinski, Q.T. Ostrom, D.D. Lightner, J.S. Barnholtz-Sloan, et al., Epidemiologic and molecular prognostic review of glioblastoma, Cancer Epidemiol. Biomarkers Prev. 23 (10) (2014 Oct) 1985–1996.
[15] B. Tran, M.A. Rosenthal, Survival comparison between glioblastoma multiforme and other incurable cancers, J. Clin. Neurosci. 17 (4) (2010 Apr) 417–421.
[16] S. Grochans, A.M. Cybulska, D. Simińska, J. Korbecki, K. Kojder, D. Chlubek, et al., Epidemiology of glioblastoma multiforme-literature review, Cancers 14 (10) (2022 May 13).
[17] A. Omuro, L.M. DeAngelis, Glioblastoma and other malignant gliomas: a clinical review, JAMA 310 (17) (2013 Nov 6) 1842–1850.
[18] D.L. Puckett, M. Alquraishi, W. Chowanadisai, A. Bettaieb, The role of PKM2 in metabolic reprogramming: insights into the regulatory roles of non-coding RNAs, Int. J. Mol. Sci. 22 (3) (2021 Jan 25).
[19] J. Chen, J. Xie, Z. Jiang, B. Wang, Y. Wang, X. Hu, Shikonin and its analogs inhibit cancer cell glycolysis by targeting tumor pyruvate kinase-M2, Oncogene 30 (42) (2011 Oct 20) 4297–4306.
[20] W. Tang, Z.-L. Liu, X.-Y. Mai, X. Qi, D.-H. Li, Q.-Q. Gu, et al., Identification of Gliotoxin isolated from marine fungus as a new pyruvate kinase M2 inhibitor, Biochem. Biophys. Res. Commun. 528 (3) (2020 Jul 30) 594–600.
[21] M. Candolfi, K.M. Kroeger, W. Xiong, C. Liu, M. Puntel, K. Yagiz, et al., Targeted toxins for glioblastoma multiforme: pre-clinical studies and clinical implementation, Anti Cancer Agents Med. Chem. 11 (8) (2011 Oct) 729–738.
[22] Q. Zhang, Q. Liu, S. Zheng, T. Liu, L. Yang, X. Han, et al., Shikonin inhibits tumor growth of ESCC by suppressing PKM2 mediated aerobic glycolysis and STAT3 phosphorylation, J. Cancer 12 (16) (2021 Jun 11) 4830–4840.
[23] H. Berman, K. Henrick, H. Nakamura, Announcing the worldwide protein Data Bank, Nat. Struct. Biol. 10 (12) (2003 Dec) 980.
[24] E. Krissinel, K. Henrick, Inference of macromolecular assemblies from crystalline state, J. Mol. Biol. 372 (3) (2007 Sep 21) 774–797.
[25] E. Krissinel, A.A. Lebedev, V. Uski, C.B. Ballard, R.M. Keegan, O. Kovalevskiy, et al., CCP4 Cloud for structure determination and project management in macromolecular crystallography, Acta Crystallogr D Struct Biol 78 (Pt 9) (2022 Sep 1) 1079–1089.
[26] S. Agnihotri, G. Zadeh, Metabolic reprogramming in glioblastoma: the influence of cancer metabolism on epigenetics and unanswered questions, Neuro Oncol. 18 (2) (2016 Feb) 160–172.
[27] H.M. Berman, J. Westbrook, Z. Feng, G. Gilliland, T.N. Bhat, H. Weissig, et al., The protein data bank, Nucleic Acids Res. 28 (1) (2000 Jan 1) 235–242.
[28] D. Lupyan, A. Leo-Macias, A.R. Ortiz, A new progressive-iterative algorithm for multiple structure alignment, Bioinformatics 21 (15) (2005 Aug 1) 3255–3263.
[29] A.D. McLachlan, Rapid comparison of protein structures, Acta Cryst. A (38) (1982) 871–873.
[30] B. Chaneton, P. Hillmann, L. Zheng, A.C.L. Martin, O.D.K. Maddocks, A. Chokkathukalam, et al., Serine is a natural ligand and allosteric activator of pyruvate kinase M2, Nature 491 (7424) (2012 Nov 15) 458–462.
[31] V. Le Guilloux, P. Schmidtke, P. Tuffery, Fpocket: an open source platform for ligand pocket detection, BMC Bioinf. 10 (2009 Jun 2) 168.
[32] S. Jasial, Y. Hu, M. Vogt, J. Bajorath, Activity-relevant similarity values for fingerprints and implications for similarity searching, F1000Res 5 (2016 Apr 6) [version 2; peer review: 3 approved].
[33] D.E.V. Pires, T.L. Blundell, D.B. Ascher, pkCSM: predicting small-molecule pharmacokinetic and toxicity properties using graph-based signatures, J. Med. Chem. 58 (9) (2015 May 14) 4066–4072.
[34] M.J. Abraham, T. Murtola, R. Schulz, S. Páll, J.C. Smith, B. Hess, et al., GROMACS: high performance molecular simulations through multi-level parallelism from laptops to supercomputers, SoftwareX 1–2 (2015 Sep) 19–25.
[35] J. Huang, S. Rauscher, G. Nawrocki, T. Ran, M. Feig, B.L. de Groot, et al., CHARMM36m: an improved force field for folded and intrinsically disordered proteins, Nat. Methods 14 (1) (2017 Jan) 71–73.
[36] D. Nayar, M. Agarwal, C. Chakravarty, Comparison of tetrahedral order, liquid state anomalies, and hydration behavior of mTIP3P and TIP4P water models, J Chem Theory Comput. 7 (10) (2011 Oct 11) 3354–3367.
[37] Hess B. P-Lincs, A parallel linear constraint solver for molecular simulation, J Chem Theory Comput. 4 (1) (2008 Jan) 116–122.
[38] T. Darden, D. York, L. Pedersen, Particle mesh Ewald: an N·log(N) method for Ewald sums in large systems, J. Chem. Phys. 98 (12) (1993) 10089.
[39] I. Aier, P.K. Varadwaj, U. Raj, Structural insights into conformational stability of both wild-type and mutant EZH2 receptor, Sci. Rep. 6 (2016 Oct 7) 34984.
[40] B.J. Grant, A.P.C. Rodrigues, K.M. ElSawy, J.A. McCammon, L.S.D. Caves, Bio3d: an R package for the comparative analysis of protein structures, Bioinformatics 22 (21) (2006 Nov 1) 2695–2696.
[41] S.K. Baidya, S. Banerjee, B. Ghosh, T. Jha, N. Adhikari, Assessing structural insights into in-house arylsulfonyl L-(+) glutamine MMP-2 inhibitors as promising anticancer agents through structure-based computational modelling approaches, SAR QSAR Environ. Res. 34 (10) (2023 Nov 3) 805–830.
[42] S. Jana, S. Banerjee, S.K. Baidya, B. Ghosh, T. Jha, N. Adhikari, A combined ligand-based and structure-based in silico molecular modeling approach to pinpoint the key structural attributes of hydroxamate derivatives as promising meprin β inhibitors, J. Biomol. Struct. Dyn. (2024 Jan 2) 1–17.
[43] L.P. Kagami, G.M. das Neves, L.F.S.M. Timmers, R.A. Caceres, V.L. Eifler-Lima, Geo-Measures: a PyMOL plugin for protein structure ensembles analysis, Comput. Biol. Chem. 87 (2020 Jun 24) 107322.
[44] P.-C. Do, E.H. Lee, L. Le, Steered molecular dynamics simulation in rational drug design, J. Chem. Inf. Model. 58 (8) (2018 Aug 27) 1473–1482.
[45] R. Tomarchio, V. Patamia, C. Zagni, L. Crocetti, A. Cilibrizzi, G. Floresta, et al., Steered molecular dynamics simulations study on FABP4 inhibitors, Molecules 28 (6) (2023 Mar 17).
[46] B.K. Mai, M.S. Li, Neuraminidase inhibitor R-125489–a promising drug for treating influenza virus: steered molecular dynamics approach, Biochem. Biophys. Res. Commun. 410 (3) (2011 Jul 8) 688–691.
[47] S. Nosé, A unified formulation of the constant temperature molecular dynamics methods, J. Chem. Phys. 81 (1) (1984) 511.
[48] W.G. Hoover, Canonical dynamics: equilibrium phase-space distributions, Phys Rev A Gen Phys 31 (3) (1985 Mar) 1695–1697.
[49] M. Parrinello, Polymorphic transitions in single crystals: a new molecular dynamics method, J. Appl. Phys. 52 (12) (1981) 7182.
[50] S. Nosé, M.L. Klein, Constant pressure molecular dynamics for molecular systems, Mol. Phys. 50 (5) (1983 Dec 10) 1055–1076.
[51] R. Singh, V.K. Bhardwaj, P. Das, D. Bhattacherjee, G.V. Zyryanov, R. Purohit, Benchmarking the ability of novel compounds to inhibit SARS-CoV-2 main protease using steered molecular dynamics simulations, Comput. Biol. Med. 146 (2022 Jul) 105572.
[52] D. Srivastava, M. Razzaghi, M.T. Henzl, M. Dey, Structural investigation of a dimeric variant of pyruvate kinase muscle isoform 2, Biochemistry 56 (50) (2017 Dec 19) 6517–6520.
[53] S. Masaki, K. Hashimoto, D. Kihara, C. Tsuzuki, N. Kataoka, K. Suzuki, The cysteine residue at 424th of pyruvate kinase M2 is crucial for tetramerization and responsiveness to oxidative stress, Biochem. Biophys. Res. Commun. 526 (4) (2020 Jun 11) 973–977.

[54] H. Matter, Selecting optimally diverse compounds from structure databases: a validation study of two-dimensional and three-dimensional molecular descriptors, J. Med. Chem. 40 (8) (1997 Apr 11) 1219–1229.
[55] M. Nakada, S. Nakada, T. Demuth, N.L. Tran, D.B. Hoelzinger, M.E. Berens, Molecular targets of glioma invasion, Cell. Mol. Life Sci. 64 (4) (2007 Feb) 458–478.
[56] C.A. Yuen, S. Asuthkar, M.R. Guda, A.J. Tsung, K.K. Velpula, Cancer stem cell molecular reprogramming of the Warburg effect in glioblastomas: a new target gleaned from an old concept, CNS Oncol 5 (2) (2016 Mar 21) 101–108.
[57] J. Mukherjee, J.J. Phillips, S. Zheng, J. Wiencke, S.M. Ronen, R.O. Pieper, Pyruvate kinase M2 expression, but not pyruvate kinase activity, is up-regulated in a grade-specific manner in human glioma, PLoS One 8 (2) (2013 Feb 25) e57610.
[58] W. Luan, Y. Wang, X. Chen, Y. Shi, J. Wang, J. Zhang, et al., PKM2 promotes glucose metabolism and cell growth in gliomas through a mechanism involving a let-7a/c-Myc/hnRNPA1 feedback loop, Oncotarget 6 (15) (2015 May 30) 13006–13018.
[59] W. Diao, X. Tong, C. Yang, F. Zhang, C. Bao, H. Chen, et al., Behaviors of glioblastoma cells in in vitro microenvironments, Sci. Rep. 9 (1) (2019 Jan 14) 85.
[60] D. Anastasiou, Y. Yu, W.J. Israelsen, J.-K. Jiang, M.B. Boxer, B.S. Hong, et al., Pyruvate kinase M2 activators promote tetramer formation and suppress tumorigenesis, Nat. Chem. Biol. 8 (10) (2012 Oct) 839–847.
[61] S. Amin, N. Adhikari, R. Agrawal, T. Jha, S. Gayen, Possible binding mode analysis of pyrazolo-triazole hybrids as potential anticancer agents through validated molecular docking and 3D-QSAR modeling approaches, Lett. Drug Des. Discov. 14 (5) (2017 Apr 6) 515–527.
[62] G. Lanka, D. Begum, S. Banerjee, N. Adhikari, Y. P, B. Ghosh, Pharmacophore-based virtual screening, 3D QSAR, Docking, ADMET, and MD simulation studies: an in silico perspective for the identification of new potential HDAC3 inhibitors, Comput. Biol. Med. 166 (2023 Nov) 107481.
[63] I. Kufareva, R. Abagyan, Methods of protein structure comparison, Methods Mol. Biol. 857 (2012) 231–257.
[64] S. Banerjee, S. Jana, T. Jha, B. Ghosh, N. Adhikari, An assessment of crucial structural contributors of HDAC6 inhibitors through fragment-based non-linear pattern recognition and molecular dynamics simulation approaches, Comput. Biol. Chem. 110 (2024 Jun) 108051.
[65] T. Abeywardana, M. Oh, L. Jiang, Y. Yang, M. Kong, J. Song, et al., CARM1 suppresses de novo serine synthesis by promoting PKM2 activity, J. Biol. Chem. 293 (39) (2018 Sep 28) 15290–15303.
[66] J.H. Park, J.-S. Lee, Y. Oh, J.S. Lee, H.E. Park, H. Lee, et al., PKM2 is overexpressed in glioma tissues, and its inhibition highly increases late apoptosis in U87MG cells with low-density specificity, Vivo 36 (2) (2022) 694–703.
[67] Z. Zhang, J. Bai, Y. Zeng, M. Cai, Y. Yao, H. Wu, et al., Pharmacology, toxicity and pharmacokinetics of acetylshikonin: a review, Pharm. Biol. 58 (1) (2020 Dec) 950–958.
[68] W. Ye, T. Liu, W. Zhang, W. Zhang, The toxic mechanism of gliotoxins and biosynthetic strategies for toxicity prevention, Int. J. Mol. Sci. 22 (24) (2021 Dec 16).
[69] K. Zahra, T. Dey, Ashish, S.P. Mishra, U. Pandey, Pyruvate kinase M2 and cancer: the role of PKM2 in promoting tumorigenesis, Front. Oncol. 10 (2020 Mar 2) 159.
[70] A. Najafov, D.R. Alessi, Uncoupling the Warburg effect from cancer, Proc. Natl. Acad. Sci. U.S.A. 107 (45) (2010 Nov 9) 19135–19136.
[71] M. Gao, J. Huang, X. Jiang, Y. Yuan, H. Pang, S. Luo, et al., Regulation of aerobic glycolysis to decelerate tumor proliferation by small molecule inhibitors targeting glucose transporters, Protein Cell 11 (6) (2020 Jun) 446–451.
[72] W. Yang, Z. Lu, Pyruvate kinase M2 at a glance, J. Cell Sci. 128 (9) (2015 May 1) 1655–1660.
[73] C.V. Dang, The interplay between MYC and HIF in the Warburg effect, Ernst Schering Found Symp Proc. (4) (2007) 35–53.
[74] A. Wolf, S. Agnihotri, D. Munoz, A. Guha, Developmental profile and regulation of the glycolytic enzyme hexokinase 2 in normal brain and glioblastoma multiforme, Neurobiol. Dis. 44 (1) (2011 Oct) 84–91.
[75] J. Liang, R. Cao, X. Wang, Y. Zhang, P. Wang, H. Gao, et al., Mitochondrial PKM2 regulates oxidative stress-induced apoptosis by stabilizing Bcl2, Cell Res. 27 (3) (2017 Mar) 329–351.